Nanoscale

PAPER

View Article Online
View Journal | View Issue

Cite this: *Nanoscale*, 2015, **7**, 8016

Preparation of Nd–Fe–B by nitrate–citrate auto-combustion followed by the reduction–diffusion process†

Hao Xuan Ma,[a] Chang Woo Kim,[a] Dong Soo Kim,[b] Ji Hun Jeong,[a] In Ho Kim[a] and Young Soo Kang*[a]

Received 20th February 2015,
Accepted 29th March 2015

DOI: 10.1039/c5nr01195g

www.rsc.org/nanoscale

The $Nd_2Fe_{14}B$ alloy has been successfully synthesized by nitrate–citrate auto-combustion followed by the reduction and diffusion process with low energy consumption. H_3BO_3, $Fe(NO_3)_3{\cdot}9H_2O$, and $Nd(NO_3)_3{\cdot}6H_2O$ were used as precursors and citric acid was used as the chelating ligand of metal ions. Ammonia water was used to adjust pH to 7. CaH_2 was used as a reducing agent for the reduction and diffusion process. $NdFeO_3$ and Fe_2O_3 were produced during auto-combustion of gel. The combustion process of the gel was investigated by TGA/DTA curve measurements. The phase compositions were studied by XRD measurements. The differences of the overall morphology and magnetic properties were measured by SEM, TEM and vibrating sample magnetometry (VSM) at 300 K. The comparison of the magnetic properties of the reduced samples between the pellet type and the random powder type was done with VSM and it showed better magnetic properties of the pellet type $Nd_2Fe_{14}B$. Making a compact pellet type sample for reduction is more efficient for solid reduction and phase transition for higher coercivity.

Introduction

High performance permanent magnets have drawn great attention in the magnetic materials research field for the past few years. Among them, the neodymium–iron–boron (Nd–Fe–B) magnet exhibits the highest magnetic maximum energy product in the category of permanent magnets.[1–3] Magnetic materials have been used in a diverse range of applications such as the parts of automobiles and ships, electronic and electrical devices, storage of data on audio and video tapes as well as on computer disks, *etc*.

Most of the studies on the synthesis of permanent magnets are focused on powder metallurgy methods,[1,4] rapid quenching techniques and the hot melt spinning process.[5,6] The Nd–Fe–B magnet synthesized *via* the mechanical synthesis route shows relatively high magnetic properties of the maximum energy product in the range of 320–440 kJ m^{-3}.[7] However, these methods need large amounts of energy. Besides, the grain size control is difficult in the nanometer range. This is also why the different kinds of HDDR (hydrogenation, disproportionation, desorption, and recombination) processes are widely used in industry for refining the grain size.[8,9] Previously, only a few researchers utilized the soft chemical route to synthesize Nd–Fe–B. It is difficult to synthesize a high performance $Nd_2Fe_{14}B$ material by a soft chemical route. The better crystallinity with the nano-size and the high reactivity of rare earth metals make the synthesis of nanoparticles a big challenge.[10] The large difference of the redox potential between the transition metal and the rare-earth metal makes the co-reduction a challenge. For example, the reduction potential of Nd^{3+}/Nd^0 is $E^0 = -2.43$ eV. It is much lower than the $E^0 = -0.44$ eV of Fe^{2+}/Fe^0. However perfect exchange coupled nanocomposites composed of soft and hard magnets can get a higher maximum energy product value. It is also easy to control the particle size by the soft chemistry method. So, the soft chemistry method to synthesize Nd–Fe–B, Sm–Co, Fe–Pt, *etc*. magnets has drawn more and more attention than the mechanical method.[11,12]

One of the recent approaches is the formation of $Nd_2Fe_{14}B$ using sodium borohydride[13] and polymeric gel decomposition followed by reduction–diffusion.[14] Previous studies also reported on the sol–gel method using citric acid and ethylene glycol or glycine.[15,16] But the magnetic properties are lower compared with the mechanical method and there is always little amount of by-products such as α-Fe, Fe–B compound, Nd–Fe compound, *etc*. It indicates that the reduction process is not perfect and it has some remaining impurities such as

[a]*Korea Center for Artificial Photosynthesis and Department of Chemistry, Sogang University, Seoul 121-742, Korea. E-mail: yskang@sogang.ac.kr; Fax: +82 2701 0967; Tel: +82 2701 6379*
[b]*Korea Institute of Material Science, Changwon, Gyeongnam 642-831, Korea*
†Electronic supplementary information (ESI) available. See DOI: 10.1039/c5nr01195g

the α-Fe particle. A large amount of α-Fe will decrease the magnetic properties such as the maximum energy product because it decreases the magnetic coercivity and remanence. So the synthesis of high performance and relatively pure $Nd_2Fe_{14}B$ materials is a big challenge for the researchers. But the exchange coupled $Nd_2Fe_{14}B$/α-Fe was focused upon in further studies by maximizing the magnetic spin exchange interaction between hard and soft phases.[17–21] For example, recently Hou *et al.* have reported a novel method with two-step thermal decomposition followed by the reductive annealing process to synthesize $Nd_2Fe_{14}B$/α-Fe nanocomposites.[17] In their work, the nanocomposite magnet of $Nd_2Fe_{14}B$/α-Fe was not mixed homogeneously. It was prepared by inserting α-Fe nanoparticles into the $Nd_2Fe_{14}B$ matrix by chemical and physical methods. Besides, the morphology of $Nd_2Fe_{14}B$ particles also can affect the magnetic properties, such as the results obtained by Swaminathan *et al.*[22] Recently, the sol–gel auto-combustion method was utilized to synthesize the homogeneous oxide powder.[23] This is a low cost method because it does not need expensive precursors and is easy to prepare.

In the present study, the auto-combustion method of citrate–nitrate gel was used to prepare the metallic oxides. The pH was adjusted by the addition of ammonia water to be 7.0. The citric acid can be chelated with metal ions to obtain a homogeneous dispersion. Beside it can also act as a fuel which is ignited by the heat of NH_3NO_3 decomposition and promotes sustained and rapid burning.[24] The reduction and diffusion process mainly affects the phase transition and the purity. From this experiment, $Nd_2Fe_{14}B$ can be obtained easily. In addition, the influence of the sample type, pellet and random powder type on the reduction step and magnetic properties has not been thoroughly discussed in any articles. So the comparative study on the reduction reaction efficiency between pellet type and random powder type samples has been carried out to obtain better magnetic properties.

Experimental

Materials

$Fe(NO_3)_3{\cdot}9H_2O$ (98%, Sigma Aldrich), $Nd(NO_3)_3{\cdot}6H_2O$ (99.9%, Aldrich Chemicals), H_3BO_3 (99.9%, Katayama Chemicals), citric acid (99.5+%, Aldrich Chemicals), CaH_2 (95%, Sigma Aldrich) and ammonia water were used as received without further purification and deionized water was used as a solvent.

Synthesis

The synthesis of Nd–Fe–B magnetic materials was carried out by the nitrate–citrate auto-combustion method. The precursors, $Fe(NO_3)_3{\cdot}9H_2O$, $Nd(NO_3)_3{\cdot}6H_2O$, H_3BO_3, were taken in the molar ratios of Nd : Fe : B – 15 : 77 : 8 for the synthesis of the $Nd_2Fe_{14}B$ material. 0.015 mol $Nd(NO_3)_3{\cdot}6H_2O$, 0.077 mol $Fe(NO_3)_3{\cdot}9H_2O$ and 0.008 mol H_3BO_3 were dissolved in 50 ml deionized water in a vial and stirred for 1 h. 0.11 mol citric acid was added to 50 ml deionized water. Then, the citric acid solution was slowly added dropwise to the above solution. To produce a stable sol, the solution was adjusted to get the pH value to be 7 by the addition of ammonia water and mixed by stirring for 2 h. The water was removed by heating the solution at 80 °C with continuous steady magnetic stirring to obtain a viscous gel. The viscous gel was dried at 220 °C for 2 h, then ignited and burned spontaneously. Excess 4 at% of Nd precursor was added to compensate for the Nd loss during the reaction. The mixed solid oxides were ground simply. The desired $Nd_2Fe_{14}B$ was then synthesized by the reduction and diffusion process. To reduce iron oxides, the solid oxide powders were reduced with Ar + 5% H_2 at 800 °C for 2 h. Then the solid powders were mixed with CaH_2 by hand grinding (the weight ratio of solid oxides to CaH_2 is 1 : 1.1) in a glove box and then a half amount of powder was weighed to prepare a compact pellet sample (CPS) with 310 kgf cm^{-2} for 40 s, and the remaining random powder sample (RPS) was used for random powder type reduction. The pellet and random powder were put in an alumina crucible and transferred to a quartz tube furnace under flowing Ar gas. The samples were annealed at 900 °C for 2.5 h for the efficient reduction and diffusion process. After annealing, the reduced samples were thoroughly washed with deionized water and then a little amount of dilute acetic acid (0.5 M) was added to remove some impurities such as CaO and $Ca(OH)_2$ for 20 min, then washed with deionized water several times. The powders were finally washed with acetone two times and stored in hexane. The simple flow diagram of the synthesis process is shown in Fig. 1.

Characterization

X-ray diffraction (XRD) patterns of the metal oxides and reduction products were measured using Cu Kα radiation (λ = 1.54056 Å) on a Rigaku MiniFlex-II desktop X-ray diffraction device with 30 kV and 15 mA. The morphologies and EDS of the samples were obtained by using a Hitachi Horiba S-4300

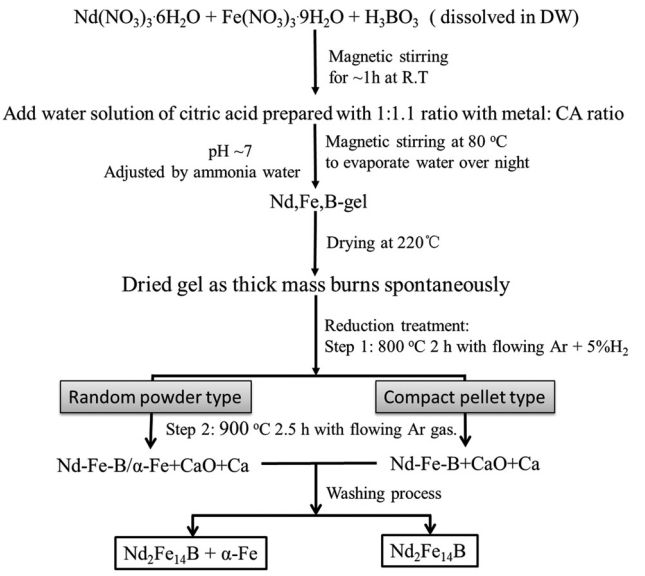

Fig. 1 Flow diagram of the Nd–Fe–B synthetic process.

and JSM-7000F, JEOL, Japan Scanning Electron Microscope (SEM) and Transmission Electron Microscope (TEM, JEOL JEM-2010). Thermogravimetric analysis (TGA) and differential thermal analysis (DTA) of the dried gel were carried out by using a STA N-650 simultaneous thermal analyzer (SCINCO) with a heating rate of 10 °C min^{-1} under air flow. The room temperature magnetic properties were measured using a vibrating sample magnetometer (VSM, LakeShore 7400).

Results and discussion

TGA/DTA curves of Nd–Fe–B oxide gel are shown in Fig. 2. The TGA and DTA curves exhibit a clear gigantic weight loss peak at around 220 °C and an intense exothermic peak, respectively. The large weight loss as much as 80% is due to the combustion reaction of the organic component (citric acid) with the nitrate, in which the citric acid and nitrate were used as the fuel and oxidant, respectively, during the combustion step. The pH was adjusted by the addition of ammonia water to 7.0. Because of the mixing of nitrate precursors and ammonia water, NH_3NO_3 is formed. So, during NH_3NO_3 decomposition, it releases a large amount of heat and O_2 as the reported reaction of $NH_4NO_3 \rightarrow 2H_2O + N_2 + [O]$,[25] which lead to the burning of citric acid. They promote each other during the whole auto-combustion process. In addition, citric acid can be chelated with metal ions to obtain a homogeneous dispersion for better phase transformation in the reduction and diffusion step.

The mixture of solid metal oxides was characterized by X-ray diffraction for the determination of the phase formation after heat treatment in an oven at 220 °C. The XRD pattern in Fig. 3 shows that the main phases are $NdFeO_3$ and Fe_2O_3. $NdFeO_3$ is an important phase for synthesis of $Nd_2Fe_{14}B$. Ramanujan's report on the free energy change of reducing

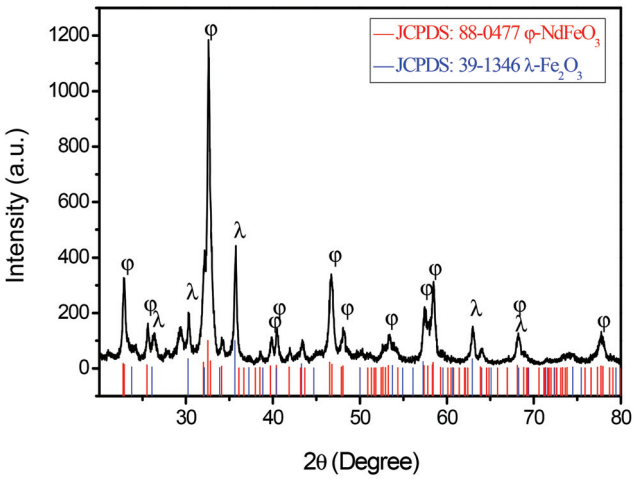

Fig. 3 X-ray diffraction pattern of the synthesized Nd–Fe–B oxides.

Nd_2O_3 to NdH_2 at ~620 °C is −21.9 kJ mol^{-1}. For the reduction of $NdFeO_3$ to NdH_2 + α-Fe by reduction with CaH_2 at ~620 °C, the free energy change is −407.5 kJ mol^{-1}.[15] So the $NdFeO_3$ phase is easier to be reduced and better for co-reduction than Nd_2O_3. The existence of boron was not detected in the XRD pattern because it is an amorphous form or in a less amount than the detection limit. Fig. 4 shows the XRD patterns of the sample after reduction treatment of Nd–Fe–B oxides. Fig. 4(a) shows the XRD pattern of the first step reduction of solid oxides. Fe_2O_3 was reduced to α-Fe as a major product. Fig. 4(b) shows the XRD pattern of the reduced sample using CaH_2 after the washing process. The dominant peaks belong to $Nd_2Fe_{14}B$. After the reduction and diffusion process at 900 °C, the $NdFeO_3$ and $NdBO_3$ were reduced and transformed to the Nd–Fe–B alloy. During this process, CaO was also formed. The

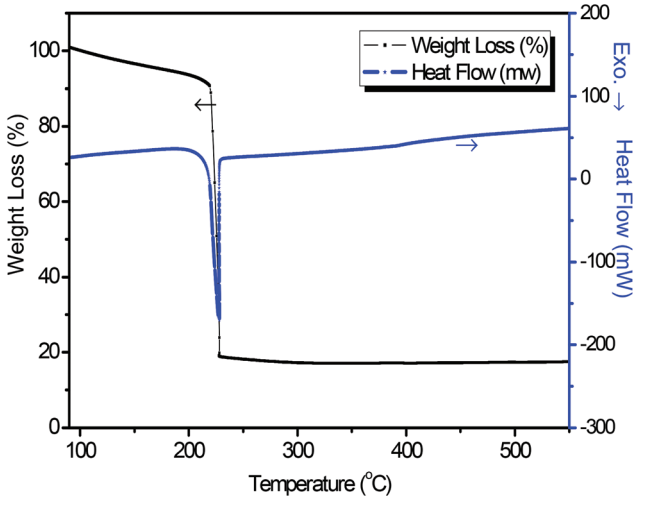

Fig. 2 DTA and TGA curves of Nd–Fe–B oxide gel obtained under an air atmosphere.

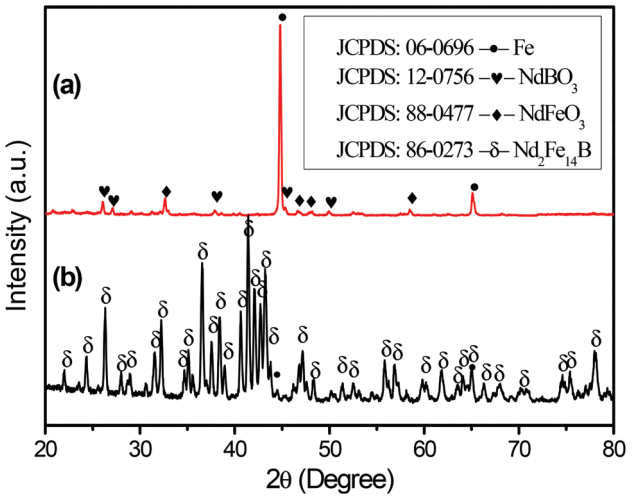

Fig. 4 X-ray diffraction patterns of powders after (a) reduction treatment at 800 °C for 2 h by Ar + 5% H_2 and (b) reduction and diffusion treatment at 900 °C for 2.5 h with CaH_2 and washing process.

reduction of the metal oxides was done as the following reaction processes (1)–(4) (M stands for metal or boron elements):[15]

$$CaH_2 \rightarrow Ca + 2H \quad (1)$$

$$M_nO_m + mCa \rightarrow nM + mCaO \quad (2)$$

$$M + xH \rightarrow MH_x \quad (3)$$

$$2H \rightarrow H_2 \quad (4)$$

SEM images of metal oxides mixed with CaH_2 (CPS and RPS) are shown in Fig. 5. The real stuff pictures of metal oxides mixed with CaH_2 of pellet and random powder types are shown in Fig. S1(a) and (b),† respectively. The SEM image in Fig. 5(a) is the surface micrograph of the pellet type sample of Nd–Fe–B oxides mixed with CaH_2, the particles are agglomerated with a diameter of 80 nm which can be seen in Fig. S2† of the only Nd–Fe–B oxide pellet surface. From the comparison of the images before and after mixing with CaH_2, it is easy to observe the existence of CaH_2 and it was compactly connected with the Nd–Fe–B oxides in the CPS. The particles were in contact with each other and there were not many voids among the Nd–Fe–B oxide particles and CaH_2. The SEM image in Fig. 5(b) shows the surface micrograph of the powder type sample. There are many voids among the Nd–Fe–B oxides and CaH_2 particles. Some CaH_2 appear isolated from Nd–Fe–B oxides. This can decrease the reduction efficiency of CaH_2. In addition, the EDS mappings and EDS spectra of RPS and CPS are shown in Fig. 6. The SEM images of selected areas of RPS and CPS are shown in Fig. 6(a) and (b), respectively. The elements are dispersed homogeneously as observed from the elemental mapping images in Fig. 6(c) RPS and (d) CPS. The CaH_2 is relatively mixed well with the Nd–Fe–B oxides. Because of the limitation of the SEM machine, the boron element is not shown in the EDS spectra in Fig. 6(e) and (f). The atomic ratios of Nd/Fe were 0.24 (Fig. 6(e)) and 0.23 (Fig. 6(f)), respectively. The amounts of Nd and Fe elements are almost close and it indicates that the elements of the metal oxides are homogeneously distributed. This point also can be obtained from the EDX mapping in Fig. 6(c) and (d). The atomic ratio between Nd and Fe elements is similar to the initial reactant ratio of Nd and Fe precursors (Nd/Fe = 0.24). The pellet type sample agglomerated with powders is better for the reduction and diffusion process because making a pellet is helpful for the compact connection of metal oxides with CaH_2. It promotes the diffusion process during the reduction process due to a larger interaction area. It also suppresses the oxidation process. XRD patterns of reduced samples are shown in Fig. 7. Fig. 7(a) and (b) are XRD patterns of the reduced samples prepared by the pellet type and powder type reduction, respectively. From the comparison of XRD peaks, it is observed that a simple hand grinding using mortar in a glove box for powder type sample reduction leads to strong Fe peaks. On the other hand, a pellet type sample reduction leads to the dominant $Nd_2Fe_{14}B$ peaks. It indicates that making a pellet is more efficient for the reduction and diffusion process to obtain the dominant $Nd_2Fe_{14}B$ phase. Quantitative analysis was performed *via* MDI Jade software and shown in Fig. S3.† For the random powder type reduction product in Fig. S3(a),† the α-Fe phase is around 40 wt%. It means that the diffusion process is not efficient because of the void space among the particles to

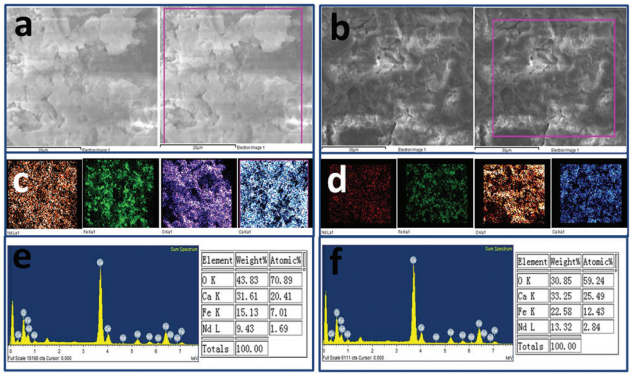

Fig. 6 SEM images of the (a) RPS and (b) CPS, EDX element mapping of the (c) RPS and (d) CPS, EDX spectrum of the (e) RPS and (f) CPS.

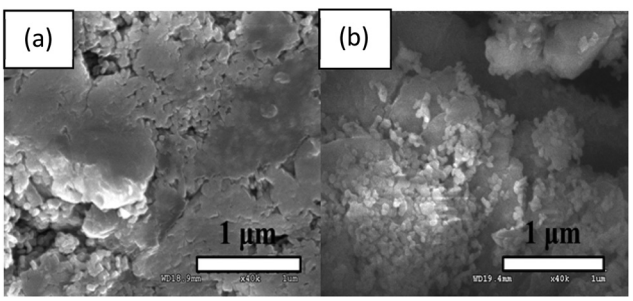

Fig. 5 SEM images of solid metal oxides mixed with CaH_2. (a) compact pellet surface, (b) random powders.

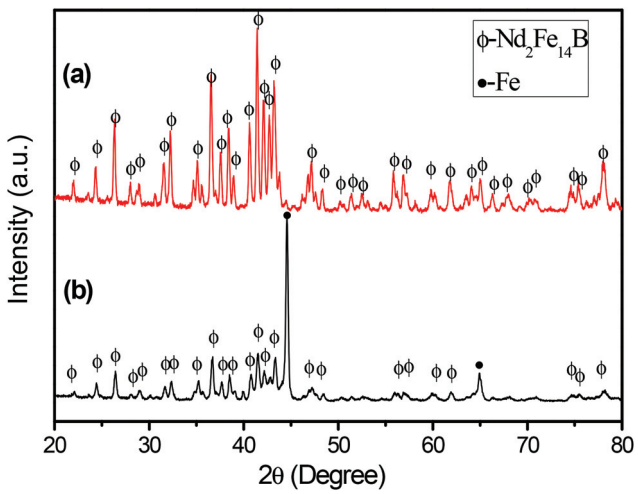

Fig. 7 XRD patterns of the reduced samples of (a) pellet type sample and (b) random powder type sample.

suppress the diffusion of Nd and Fe elements for the formation of the $Nd_2Fe_{14}B$ phase and it will result in a low magnetic coercivity. For the pellet type reduction sample in Fig. S3(b),† Fe peaks are not detectable which indicates a very low wt% of α-Fe and an almost dominant $Nd_2Fe_{14}B$ phase. Even in the powder type sample of $Nd_2Fe_{14}B$, 40 wt% of α-Fe particles were not homogeneously distributed into the $Nd_2Fe_{14}B$ particles. It is clearly shown by the low magnetic properties ($(BH)_{max}$ value) of the powder type sample as shown in Fig. 8. The homogeneously distributed 3-dimensional exchange coupled α-Fe/$Nd_2Fe_{14}B$ nanocomposite magnet will be reported in the further study.

Magnetic properties of the two kinds of reduced samples were studied by VSM measurements. The *M–H* hysteresis curves of the reduced $Nd_2Fe_{14}B$ samples at 300 K with VSM measurements are presented in Fig. 8. The hysteresis curves belong to the pellet type reduction sample before washing (a), the pellet type reduction sample after washing (b) and the random powder type reduction sample after washing (c), respectively. The inset shows the enlarged view of the hysteresis loops at low magnetic field. It is easy to confirm the detailed magnetic property values. For the *M–H* hysteresis curves (a) and (b), the coercivity decreasing from 3407.1 G to 3283.0 G can be caused by the formation of Nd–Fe–B hydride and surface oxidation of Nd–Fe–B during the washing process. But the remanence and magnetization values increased largely, because of the removal of non-magnetic phases of Ca and CaO. The purity of the hard phase $Nd_2Fe_{14}B$ is a critical parameter to obtain high coercivity and magnetic remanence values. In this study, the more critical parameter for higher coercivity is to suppress the void space among the Nd–Fe–B oxides and CaH_2 particles which suppresses the diffusion of elements during the reduction process. In the previous articles,[26,27] it is mentioned that the formation of $Nd_2Fe_{14}BH_x$ ($x \leq 5$) occurred as a by-product and it reduces the magnetic properties of the $Nd_2Fe_{14}B$. The residual Ca metal can react with water and produce activated H which leads to the hydrogenation of the produced $Nd_2Fe_{14}B$. The formation of hydride of $Nd_2Fe_{14}B$ leads to a low magnetic property ($(BH)_{max}$ value). The detailed information has already been explained in the previous study.[28] However, the hydrogenation and dehydrogenation processes are useful in the future development for the synthesis of $Nd_2Fe_{14}B$. Moreover, from VSM results in Fig. 8, it is known that the sample *via* the pellet type reduction process showed hard magnetic properties with a larger coercivity than 1000 G. The magnetic hysteresis curves in Fig. 8(b) and (c) show that the coercivities were determined as 3283.0 and 285.76 G and the remanence values were determined as 68.99 and 19.14 emu g^{-1}, respectively. Moreover, the highest $(BH)_{max}$ value of 5.4 MGOe was obtained for the pellet type reduction sample compared to the random powder type reduction sample of 0.1 MGOe. These magnetic property values of the Nd–Fe–B magnet could be increased to much higher ones *via* the typical process of hard magnet production processes such as hot-melt pressing and one-axis magnetization with a strong external magnetic field to obtain a high density compact magnet.[8,29,30] It was identified that the pellet type sample reduction was better to prepare the hard phase $Nd_2Fe_{14}B$ than random type powder reduction. The magnetic hysteresis loop in Fig. 8(b) shows a larger coercivity and remanence because of the dominant phase of $Nd_2Fe_{14}B$. For random powder type sample reduction, a large portion of α-Fe and a small portion of $Nd_2Fe_{14}B$ were produced from the observation of XRD patterns in Fig. 7. α-Fe is a soft magnetic material which has a weak coercivity value and a large amount of it could be considered as an impurity. This can decrease the overall magnetic properties. Therefore, it was identified that the hard phase $Nd_2Fe_{14}B$ can be successfully synthesized *via* the pellet type sample reduction process than the random type powder reduction process.

SEM and TEM detection results of the washed pellet reduction product are shown in Fig. 9. The SEM image shows that the aggregate particle size is around 0.6–1.0 μm. The TEM image reveals that the particle size ranges from 100 to 150 nm

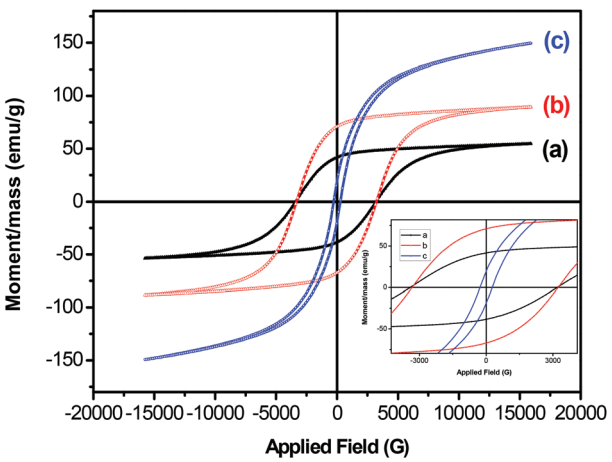

Fig. 8 The magnetic hysteresis loops of reduction product of the Nd–Fe–B alloy in the full magnetic field range at 300 K; the pellet type sample reduction product before washing (a) and after washing (b); the random powder type sample reduction product after washing (c). The inset shows the enlarged view of magnetic hysteresis loops at low magnetic field.

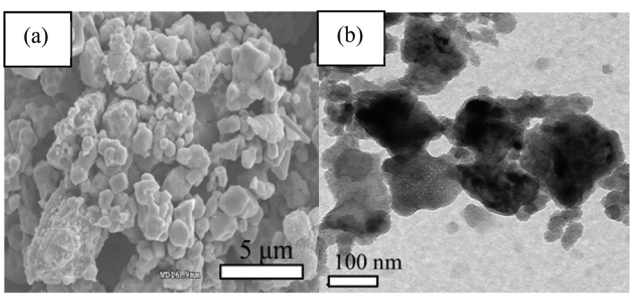

Fig. 9 SEM (a) and TEM (b) images of the pellet type reduction product of $Nd_2Fe_{14}B$ powder.

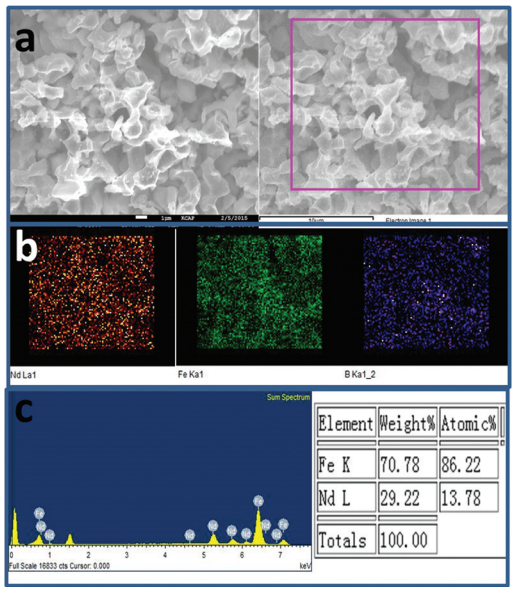

Fig. 10 SEM image (a), EDX-mapping (b) and EDX of the washed pellet type reduction product Nd–Fe–B powders (c).

with some exception of chippings of size <0 nm. The crystal size calculated from the XRD pattern by JADE software is around 44.2 nm, as shown in Fig. S4.† The SEM-EDS detection results are shown in Fig. 10. For the selected area in Fig. 10(a), the elements are dispersed well as observed from the elemental mapping images in Fig. 10(b). From the EDS spectrum measurement, the atomic ratio of Nd/Fe = 0.16 and it is slightly lower than the initial reactant ratio of Nd and Fe precursors and higher than the standard ratio of the $Nd_2Fe_{14}B$ compound (Nd/Fe = 0.14), because a small amount of Nd is lost during 900 °C reduction and washing processes. The powder shape and size are not uniform, but this study confirms that the nitrate–citrate auto-combustion followed by the reduction and diffusion method can be used for the synthesis of $Nd_2Fe_{14}B$ with nano-sized particles and synthesis of the crystallized rare permanent magnet is a potential way for continuous studies.[31–33]

Conclusions

In summary, the permanent magnet $Nd_2Fe_{14}B$ nanoparticle alloy can be successfully synthesized by the nitrate–citrate auto-combustion followed by the reduction and diffusion process. This synthesis process is easy for the production of $Nd_2Fe_{14}B$ without consuming a large amount of energy. Through the citrate–nitrate process, the Nd–Fe–B oxides ($NdFeO_3$, Fe_2O_3, B–O) were produced in a few hours. Because of the reducing capacity of CaH_2, the Nd–Fe–B oxides were transformed to $Nd_2Fe_{14}B$ at 900 °C. Moreover, it was revealed that the difference between the pellet type sample reduction process and the random powder type sample reduction process resulted in different magnetic properties and phase ratios. The pellet type sample reduction process gives a larger coercivity of 3283.0 G than that of the random powder type sample reduction process as 285.76 G and a higher $(BH)_{max}$ value of 5.4 MGOe. From XRD patterns of the reduced products, it can be shown that, after random powder type reduction, the product has a larger portion of α-Fe than the pellet reduction process. Compared with the random powder sample, the pellet type sample has much less void space among the particles. Obviously, making a compact pellet for reduction is more efficient for solid sample reduction and phase transition to obtain higher magnetic properties due to better diffusion and higher suppression for oxidation during the washing process.

Acknowledgements

The authors appreciate the financial support from the Joint Research Project of ISTK (Korea Research Council for Industrial Science and Technology) and Development in Interface Technology of Magnetoelectric Material Project.

Notes and references

1 M. Sagawa, S. Fujimura, N. Togawa, H. Yamamoto and Y. Matsuura, *J. Appl. Phys.*, 1984, **55**, 2083–2087.
2 J. M. D. Coey, *Solid State Commun.*, 1997, **102**, 101–105.
3 E. Burzo, *Rep. Prog. Phys.*, 1998, **61**, 1099–1266.
4 K. J. Strnat and R. M. W. Strnat, *J. Magn. Magn. Mater.*, 1991, **100**, 38–56.
5 J. J. Croat, J. F. Herbst, R. W. Lee and F. E. Pinkerton, *J. Appl. Phys.*, 1984, **55**, 2078–2082.
6 N. C. Koon and B. N. Das, *J. Appl. Phys.*, 1984, **55**, 2063–2066.
7 Y. Kanko, *IEEE Trans. Magn.*, 2000, **36**, 3275–3278.
8 D. Brown, B. M. Ma and Z. Chen, *J. Magn. Magn. Mater.*, 2002, **248**, 432–440.
9 R. Setnescu, T. Setnescu, S. Jipa, W. Kappel, M. Dumitru, M. M. Codescu, N. Stancu and T. J. Zaharescu, *Optoelectron. Adv. Mater.*, 2006, **8**, 533–536.
10 C. N. Chinnasamy, J. Y. Huang, L. H. Lewis, B. Latha, C. Vittoria and V. G. Harris, *Appl. Phys. Lett.*, 2008, **93**, 032505.
11 S. H. Sun, C. B. Murray, D. Weller, L. Folks and A. Moser, *Science*, 2000, **287**, 1989–1992.
12 H. W. Zhang, S. Peng, C. B. Rong, J. P. Liu, Y. Zhang, M. J. Kramer and S. H. Sun, *J. Mater. Chem.*, 2011, **21**, 16873–16876.
13 C. W. Kim, Y. H. Kim, U. Pal and Y. S. Kang, *J. Mater. Chem. C*, 2013, **1**, 275–281.
14 J. H. Lin, S. F. Liu, Q. M. Cheng, X. L. Qian, L. Q. Yang and M. Z. Su, *J. Alloys Compd.*, 1997, **249**, 237–241.
15 P. K. Deheri, V. Swaminathan, S. D. Bhame, Z. W. Liu and R. V. Ramanujan, *Chem. Mater.*, 2010, **22**, 6509–6517.
16 A. P. Jadhav, A. Hussain, J. H. Lee, Y. K. Baek, C. J. Choi and Y. S. Kang, *New J. Chem.*, 2012, **36**, 2405–2411.

17 L. Q. Yu, C. Yang and Y. L. Hou, *Nanoscale*, 2014, **6**, 10638–10642.
18 F. Liu, Y. L. Hou and S. Gao, *Chem. Soc. Rev.*, 2014, **43**, 8098–8113.
19 Y. L. Hou, Z. C. Xu, S. Peng, C. B. Rong, J. P. Liu and S. H. Sun, *Adv. Mater.*, 2007, **19**, 3349–3352.
20 S. D. Bhame, V. Swaminathan, P. K. Deheri and R. V. Ramanujan, *Adv. Sci. Lett.*, 2010, **3**, 174–179.
21 H. G. Cha, Y. H. Kim, C. W. Kim, H. W. Kwon and Y. S. Kang, *J. Phys. Chem.*, 2007, **111**, 1219–1222.
22 V. Swaminathan, P. K. Deheri, S. D. Bhame and R. V. Ramanujan, *Nanoscale*, 2013, **5**, 2718–2725.
23 M. P. Pechini, *U. S. Patent*, 3330697, 1967.
24 X. W. Qi, J. Zhou, Z. X. Yue, Z. L. Gui and L. T. Li, *Mater. Chem. Phys.*, 2003, **78**, 25–29.
25 J. L. Liu, Y. W. Zeng, C. J. Guo, W. Zhang and X. W. Yang, *J. Eur. Ceram. Soc.*, 2010, **30**, 993–997.
26 D. Fruchart, L. Pontonnier, F. Vaillant, J. Bartolomé, J. M. Fernández, J. A. Puertolas, C. Rillo, J. R. Regnard, A. Yaouanc, R. Fruchart and P. L'Héritier, *IEEE Trans. Magn.*, 1988, **24**, 1641–1643.
27 B. Rupp, A. Resnik, D. Shaltiel and P. Rogi, *J. Mater. Sci.*, 1988, **23**, 2133–2141.
28 S. Ram, *J. Mater. Sci.*, 1997, **32**, 4133–4148.
29 G. W. Jewell, *The computer aided design and analysis of impulse magnetizing fixtures*, 1992.
30 C. B. Rong, Y. Zhang, N. Poudyal, D. Wang, M. J. Kramer and J. P. Liu, *J. Appl. Phys.*, 2011, **109**, 07A735.
31 C. Yang, L. H. Jia, S. G. Wang, C. Gao, D. W. Shi, Y. L. Hou and S. Gao, *Sci. Rep.*, 2013, **3**, 3542.
32 Q. Zhang, Z. Jiang and B. Yan, *Inorg. Chem. Front.*, 2014, **1**, 384–388.
33 L. P. Jia and B. Yan, *Mater. Res. Bull.*, 2015, **64**, 93–96.